Journal of Human Evolution 76 (2014) 26–38

Contents lists available at ScienceDirect

Journal of Human Evolution

journal homepage: www.elsevier.com/locate/jhevol

The geology and chronology of the Acheulean deposits in the Mieso area (East-Central Ethiopia)

Alfonso Benito-Calvo [a, *], Dan N. Barfod [b], Lindsay J. McHenry [c], Ignacio de la Torre [d, *]

[a] Centro Nacional de Investigación sobre la Evolución Humana (CENIEH), Paseo Sierra de Atapuerca 3, Burgos 09002, Spain
[b] Natural Environmental Research Council (NERC) Argon Isotope Facility, Scottish Universities Environmental Research Centre (SUERC), Rankine Avenue, East Kilbride G750QF, United Kingdom
[c] Department of Geosciences, University of Wisconsin- Milwaukee, 3209 North Maryland Ave., Milwaukee, WI 53211, United States
[d] Institute of Archaeology, University College London, 31–34 Gordon Square, London WC1H 0PY, United Kingdom

ARTICLE INFO

Article history:
Received 10 February 2014
Accepted 26 August 2014
Available online 17 October 2014

Keywords:
Alluvial sequence
$^{40}Ar/^{39}Ar$ dating
Tephrochemistry
Pleistocene
SE Afar margin

ABSTRACT

This paper presents the Quaternary sequence of the Mieso area of Central-East Ethiopia, located in the piedmont between the SE Ethiopian Escarpment and the Main Ethiopian Rift-Afar Rift transition sector. In this region, a piedmont alluvial plain is terraced at +25 m above the two main fluvial courses, the Mieso and Yabdo Rivers. The piedmont sedimentary sequence is divided into three stratigraphic units separated by unconformities. Mieso Units I and II contain late Acheulean assemblages and a weakly consolidated alluvial sequence, consisting mainly of fine sediments with buried soils and, to a lesser degree, conglomerates. Palaeo-wetland areas were common in the alluvial plain, represented by patches of tufas, stromatolites and clays. At present, the piedmont alluvial surface is preserved mainly on a dark brown soil formed at the top of Unit II. Unit III corresponds to a fluvial deposit overlying Unit II, and is defined by sands, silty clays and gravels, including several Later Stone Age (LSA) occurrences. Three fine-grained tephra levels are interbedded in Unit I (tuffs TBI and TA) and II (tuff CB), and are usually spatially-constrained and reworked. Argon/argon ($^{40}Ar/^{39}Ar$) dating from tuff TA, an ash deposit preserved in a palustrine environment, yielded an age of 0.212 ± 0.016 Ma (millions of years ago). This date places the top of Unit I in the late Middle Pleistocene, with Acheulean sites below and above tuff TA. Regional correlations tentatively place the base of Unit I around the Early-Middle Pleistocene boundary, Unit II in the late Middle Pleistocene and within the Late Pleistocene, and the LSA occurrences of Unit III in the Late Pleistocene–Holocene.

Introduction

Late Cenozoic sedimentary sequences in the Ethiopian Rift basins have been intensively investigated since the 1980s (WoldeGabriel et al., 2000). These deposits contain renowned palaeoanthropological sites and, with the exception of some Miocene areas, belong mostly to the Plio-Pleistocene (Tiercelin, 1990; WoldeGabriel, 2012). Thick stratigraphic and palaeoanthropological sequences are concentrated particularly in the southwestern basin of the Afar Depression, near the junction of the Red Sea Rift and the Main Ethiopian Rift axes, e.g., the Middle Awash, Gona, Dikika, Hadar, Woranso-Mille, and other areas (Quade et al., 2008; Wynn et al., 2008; Deino et al., 2010; Campisano, 2012; WoldeGabriel, 2012). However, the southeastern margin of the Afar Rift and its connection with the Main Ethiopian Rift (MER) has received less attention, probably due to younger ages and poor exposure of sediments compared with areas on the Afar Rift floor (WoldeGabriel et al., 2000). Consequently, the sedimentary and archaeological record from this area is known principally from fluvial and palustrine Late Pleistocene–Holocene deposits (Abebe and Coltorti, 2011), including Later Stone Age (LSA) and Middle Stone Age (MSA) occurrences (Aladi Springs site, Clark and Williams, 1978), in addition to Miocene (Suwa et al., 2007) and Acheulean occurrences located closer to the Main Ethiopian Rift (Arba site, Clark and Williams, 1978).

Herein, we describe a new sedimentary sequence located in the junction between the northern sector of the MER and the SW Afar Rift floor, around the town of Mieso (Oromia Region, Ethiopia; WGS84 coordinates: 9°13′59.76″N 40°45′13.26″E). Our surveys in the Mieso area characterized a 24 m thick detrital succession with

* Corresponding authors.
E-mail addresses: alfonso.benito@cenieh.es (A. Benito-Calvo), i.torre@ucl.ac.uk (I. de la Torre).

http://dx.doi.org/10.1016/j.jhevol.2014.08.013
0047-2484/

palustrine patches, deposited over the foothills of the SE margin of the Afar rift. The sequence contains fossils and stone tools assigned to the Late Acheulean, LSA, and potentially also to the MSA. A detailed description and interpretation of the Mieso Middle Pleistocene archaeological sequence is presented elsewhere (de la Torre et al., Accepted), while this report details the geology and geochronology of the Mieso area. This includes a geomorphological and stratigraphic study of the Mieso sequence, with particular emphasis on the context of the archaeological findings, as well as argon–argon ($^{40}Ar/^{39}Ar$) radiometric dating and geochemical analysis of volcanic tuffs. Our results allow the alluvial sequence deposited across the Mieso area during the Middle Pleistocene and around the Late Pleistocene–Holocene boundary to be reconstructed.

Geological setting

The structural setting of the Afar Depression is defined by a rift–rift–rift triple junction (R-R-R) where the MER, southern Red Sea Rift and western Gulf of Aden Rift converge (Fig. 1A), separating the Nubian, Arabian and Somalian Plates (Wolfenden et al., 2004; Beyene and Abdelsalam, 2005). The Mieso area is located along the foothills of the SE Afar rift margin (Fig. 1B), where the MER and the Gulf of Aden Rift join together. This area is interpreted as an accommodation zone (Tesfaye et al., 2003), characterised by a gradual structural transition from the NE–SW-trending eastern margin of the northern sector of the MER, to the E–W-trending southern boundary fault of the Gulf of Aden Rift (Juch, 1980; Berhe, 1986, Fig. 1C). Based on this structural variation, Tesfaye et al. (2003) propose that the MER-Gulf of Aden Rift floor boundary runs between the Asebot and the Afdem volcanoes, precisely across the Mieso area. Towards the south-east, the Mieso study area is delimited by the SE Afar rift margin (Fig. 1B), where the regional structural features include closely spaced, short-segmented normal faults, changing from antithetic to synthetic (Berhe, 1986; Tesfaye et al., 2003). In the rift floor, the Mieso area is delimited to the west by the NNE-SSW trending Wonji fault belt that represents the continuation of the MER in the Afar Depression (Abebe et al., 2005, 2007). The fault belt exhibits segmented normal faults (Tesfaye et al., 2003), parallel grabens and fissures with basalt cinder cones and lava fields along with several volcanoes and calderas distributed along the rift floor parallel to the main structural trend (Chernet et al., 1998).

Lithological units in this area begin with the Late Proterozoic Metamorphic Complex (Fig. 1C), which is exposed along the SE Afar rift margin and the SE Ethiopian Plateau and underlies the Triassic,

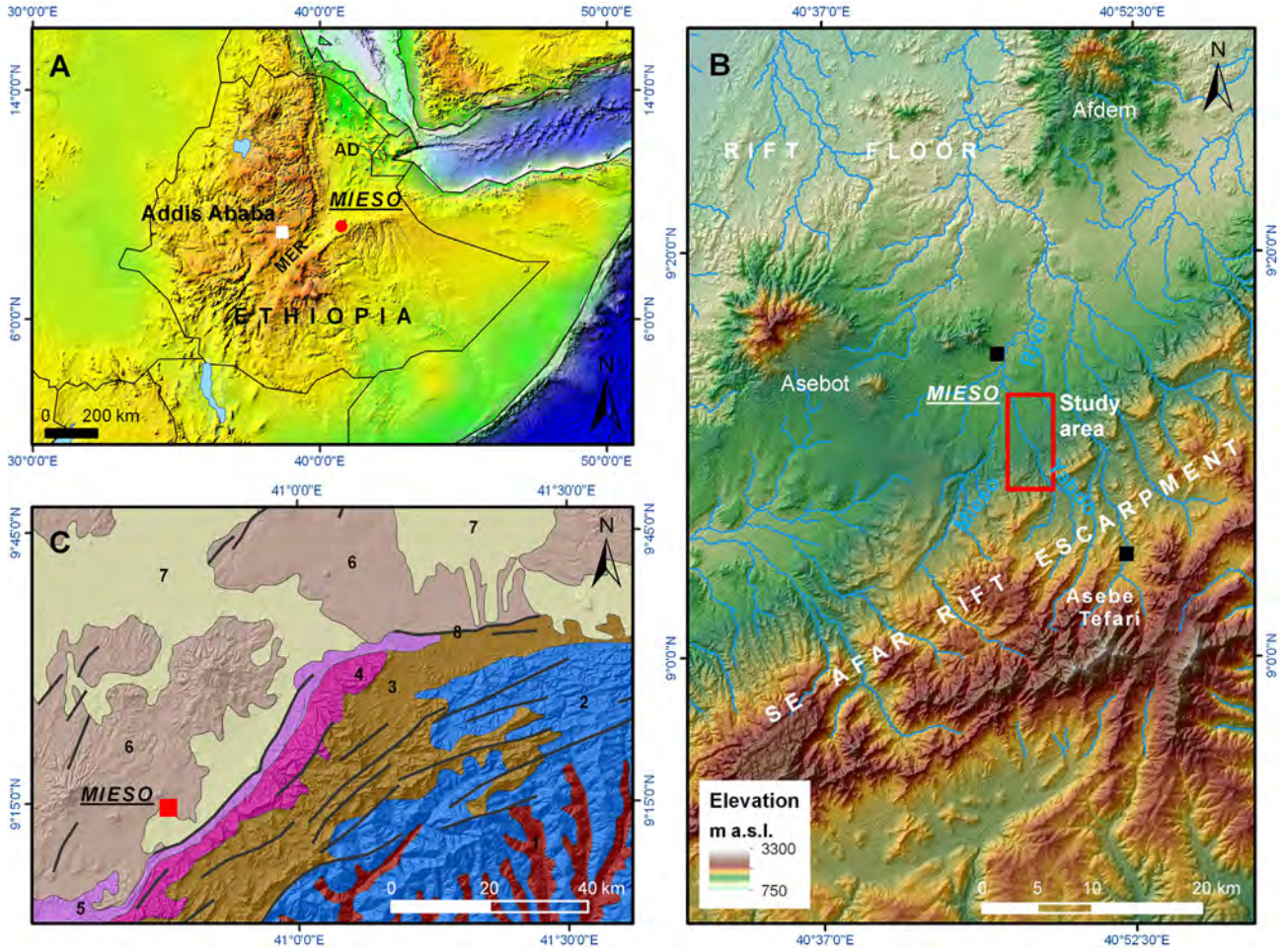

Figure 1. Regional location of the Mieso study area. A) Location of Mieso in the East-Central sector of Ethiopia, in the transition area between the southern Afar Depression (AD) and the Main Ethiopian Rift (MER). B) GDEM model showing the position of the Mieso study area in the SE Afar rift margin piedmont, drained by the Mieso and Yabdo Rivers. C) Mieso geological location in the accommodation zone between the MER and the Gulf of Aden Rift (modified after Berhe, 1986; Tesfaye et al., 2003). Legend: 1, Late Proterozoic Metamorphic Complex; 2, Mesozoic sedimentary rocks; 3, Alaje basalts; 4, Arba Guracha silicic volcanics; 5, Anchar basalts; 6, Basalts, trachytes and rhyolites of the rift floor; 7, Quaternary alluvial sediments; 8, Major faults. Map geographic coordinate system: WGS84.

Jurassic and Cretaceous sedimentary rocks (Tefera et al., 1996). Oligocene-Miocene volcanic rocks also crop out along the escarpment, and include basalts and, to a lesser degree, rhyolites, trachytes and ignimbrites from the Alaje, Arba Guracha and Anchar units (Berhe, 1986; Tefera et al., 1996; Chernet et al., 1998). The Late Miocene Chorora Formation (Suwa et al., 2007) is located to the south-west of the Mieso Valley, as is the Arba area, where Clark and Williams (1978) reported fluvial gravels with Upper Acheulean stone tools overlying Pliocene lacustrine deposits. Lithologies exposed on the rift floor of the Mieso Valley include the Miocene-Pliocene Afar series (basalts and peralkaline silicic volcanic rocks), the Pliocene Chilalo Formation (trachyte, trachy-basalts and rhyolites), and undifferentiated Pleistocene-Holocene alluvial sediments (Berhe, 1986; Tefera et al., 1996).

An extensive pediment is developed on the faulted blocks of the SE Afar rift margin, much of which is incised more than 200 m deep by fluvial erosion (Coltorti et al., 2011a, b). The pediment was covered by the Afar stratoid series before a second phase of pedimentation took place (Abebe and Coltorti, 2011). This second pediment is interpreted as Late Pleistocene in age, and is itself covered by alluvial sediments currently terraced 10 m above the valley floor, which include an organic-rich soil dated at 35,080 ± 280 years BP (before present) (Berak stratigraphic unit; Abebe and Coltorti, 2011). The sediments are unconformably capped by a second stratigraphic unit (Uabi Adakaloya unit) containing several tufas from the Late Pleistocene (16,810 ± 100 years BP) and Holocene (from 9120 ± 50 to 6200 ± 40 years BP). To the north-east of Mieso is the Aladi Springs site, where a tufa level exists with LSA industry and abundant gastropod shells, dated at 11,070 ± 160 years BP (Williams et al., 1977; Clark and Williams, 1978). Middle Stone Age assemblages have been reported below the tufa level (Clark and Williams, 1978; Gossa et al., 2012).

Materials and methods

Field studies: geomorphology and stratigraphy

Geomorphological and stratigraphic data points obtained during fieldwork were recorded using a handheld GPS. Field surveys were augmented by analysis of aerial photographs and 1:50,000 maps from the Ethiopian Mapping Authority, Landsat TM and Google Earth imagery, and Digital Elevation Models (DEM) corresponding to the SRTM90 and ASTER GDEM databases. Data points were georeferenced and analysed using Geographical Information Systems (ArcGIS 10.2). In outcrops associated with archaeological sites, stratigraphic logs and sections were recorded using a total station. Sedimentary sequences were divided into unconformity-bounded stratigraphic units (Murphy and Salvador, 1999).

Tephrochemistry: electron microprobe analysis

Tephra samples were gently crushed in a ceramic mortar and pestle and sieved, with the 150 μm size fraction selected for further processing. The sieved sample was washed in 4% HF (hydrofluoric acid) in an ultrasonic bath for 1 min, then rinsed three or more times in deionised (DI) water and dried for about 15 min under a heat lamp. Individual glass shards were hand picked under a binocular microscope and mounted in epoxy. The mounts were polished and carbon coated, then analysed by electron probe microanalysis (EPMA) using a Cameca SX50 at the University of Wisconsin–Madison. The glass shards were analysed at 15 kV, 10 nA, with a 5 μm spot size. Kakanui hornblende was used as the calibration standard. Sample preparation and analysis methods are presented in greater detail in McHenry et al. (2011).

Laboratory studies: $^{40}Ar/^{39}Ar$ dating

Several tuff samples were collected for $^{40}Ar/^{39}Ar$ dating. Samples were gently crushed and sieved, selecting the 250–500 μm fraction for further preparation. A strong hand magnet (wrapped in paper) was passed over the crushed material to remove metal particles introduced by the crushing process. The samples were rinsed in DI and then more thoroughly washed in DI in an ultrasonic bath for 10 min, followed by drying at T ≤ 100 °C. A magnetic separator was used to remove glass and other sediments, to produce a feldspar-rich split. The feldspar split was leached in $3N \cdot HNO_3$ for 10 min in an ultrasonic bath at 50 °C; if the acid was significantly cloudy (i.e., opaque at 2 cm thickness/depth) the HNO_3 step was repeated until a relatively clear solution was obtained. The feldspar aliquot was further leached in 5% VOL HF for 5 min to remove any residual adhering glass or surficial alteration. The samples were rinsed three times in DI to halt the leaching, and then more thoroughly washed in DI in an ultrasonic bath for 10 min, followed by a second drying at T ≤ 100 °C. The final stage of preparation involved hand picking under a binocular microscope to remove altered grains and those with numerous inclusions, in an effort to produce a homogeneous, clean feldspar separate.

Prepared samples and neutron flux monitors were placed in aluminium discs and stacked in quartz tubes for irradiation. The relative positions of wells in the discs were precisely measured for later reconstruction of neutron flux gradients. The sample package was irradiated in the Oregon State University reactor, Cd-shielded CLICIT facility. Alder Creek Sanidine (1.2056 ± 0.0019 Ma, Renne et al., 2011) was used to monitor ^{39}Ar production and establish neutron flux values (J) for the samples. The neutron flux within a given disc was calculated by least-squares fitting of a surface to the J-monitors. Estimated errors (generally <0.5%) in the neutron flux measurements were calculated from the residual deviation from the fitted surface.

Individual sample grains were loaded into a steel planchette containing 208 2 mm in diameter wells for analysis. Gas was extracted from samples using a mid-infrared CO_2 laser delivering ~3.75 W focused to a spot size of ~1 mm, with samples housed in a ZnS-window laser cell. Liberated argon was then purified of active gases (e.g., CO_2, H_2O, H_2, N_2, CH_4) using three Zr–Ti–Al getters; one at 25 °C and two at 400 °C. Data were collected on a GVi instruments ARGUS 5 multi-collector mass spectrometer using a variable sensitivity faraday collector array in static collection (non-peak hopping) mode (Sparks et al., 2008; Mark et al., 2009). Time-intensity data were regressed to t_0 with second-order polynomial fits to the data. Mass discrimination was monitored by comparison to running-average values of an air standard. The average total system blanks for laser extractions, measured between each sample run, were 6.7×10^{-16} mol ^{40}Ar, 1.1×10^{-17} mol ^{39}Ar, and 2.5×10^{-18} mol ^{36}Ar. All data were blank, interference and mass discrimination corrected. Decay constant values are those listed in Renne et al. (2011), and a value for $^{40}Ar/^{36}Ar_{ATM} = 298.56 \pm 0.31$ is assumed (Lee et al., 2006; Mark et al., 2009).

Results: the Mieso Quaternary sequence

Geomorphology

The Mieso area is located in the piedmont slope between the SE Afar Rift margin and the rift floor (Fig. 1B), in the area connecting the southern Afar and the MER Depressions (Ethiopia). The SE margin is characterised by faulted blocks tilted towards the rift depression. Oligocene to Lower Miocene volcanic materials form monoclinal ramps that dip 2–4° and are degraded and incised by a drainage network. The main drainage channels in the study area are

the Mieso and Yabdo Rivers (Fig. 1B). These rivers and their tributaries flow from the SE Ethiopian Plateau (2000–3000 m above sea level [a.s.l.]) down to the rift floor (750–800 m a.s.l.) and erode valleys in a SE–NW direction, incised near 400–500 m into the SE Afar Escarpment. On the rift floor, the SE–NW flowing trends change to N and NNE directions bounded by the Sufi (1640 m a.s.l.) and Afdem volcanoes (2125 m a.s.l.).

An aggradational landform is developed in both the valleys and along the foothills of the rift margin. This landform is formed by coalescence of alluvial sediments forming a gentle piedmont alluvial plain (Fig. 2). This piedmont extends from the escarpment valleys (1700 m a.s.l. near Asebe Tefari), dipping 3–4° toward the rift floor (1320 m a.s.l. in the surroundings of Mieso town), where the slope decreases to 1.0–1.5°. The piedmont is dissected and terraced by a drainage network and hangs 25 m above the present valley floors (Fig. 2B). Incision by the Mieso and Yabdo Rivers has partially eroded sediments from this depositional plain, exposing a sequence with a maximum thickness of 24 m. This sequence comprises alluvial-colluvial deposits in the foothills, while in the depressions there are mainly alluvial sediments and, to a lesser degree, palustrine sediments and fallout volcanic ashes. These deposits lie unconformably on volcanic bedrock (basalts and welded tuffs) that is typically weathered. At the escarpment, the dissection of the piedmont alluvial plain by the rivers produces steep gorges. In contrast, valley incision in the depression shows variable geometry; the upper slopes of the valleys cut unevenly through the sedimentary sequence and show wider geometries that include lateral badlands and gullies, whereas the lower parts form narrow gorges 2–4 m wide and 5–10 m deep, carved into the volcanic bedrock (Fig. 3). Additionally, a recent fluvial terrace hangs 4–5 m above the Mieso River channel.

Stratigraphy

The alluvial piedmont stratigraphic sequence was studied in an area of 10.1 km^2 across the Mieso and Yabdo Valleys and their tributaries (Fig. 2A) that had previously been selected for analysis using remote sensing on Landsat TM, Google Earth imagery and GDEM datasets. In general, all areas are partially covered by vegetation, but the visible outcrops reveal an alluvial succession where light yellow and dark grey fine-grained detrital deposits dominate over coarse sediments. Archaeological findings are usually Acheulean, as evidenced by the presence of handaxes (de la Torre et al., Accepted). The top of these sediments is marked by a dark brown soil that contains putative MSA occurrences in Area 9 (Fig. 2A). More recent sediments including LSA assemblages were documented in Area 2 as well. A detailed stratigraphic study of the sedimentary sequence focused on the areas with better-exposed outcrops (Areas 1, 2 and 7, Fig. 2B) enabling identification of three stratigraphic units bounded by unconformities.

Area 1 This area is located to the immediate southeast of Mieso town, in the confluence of the Mieso and Yabdo Rivers

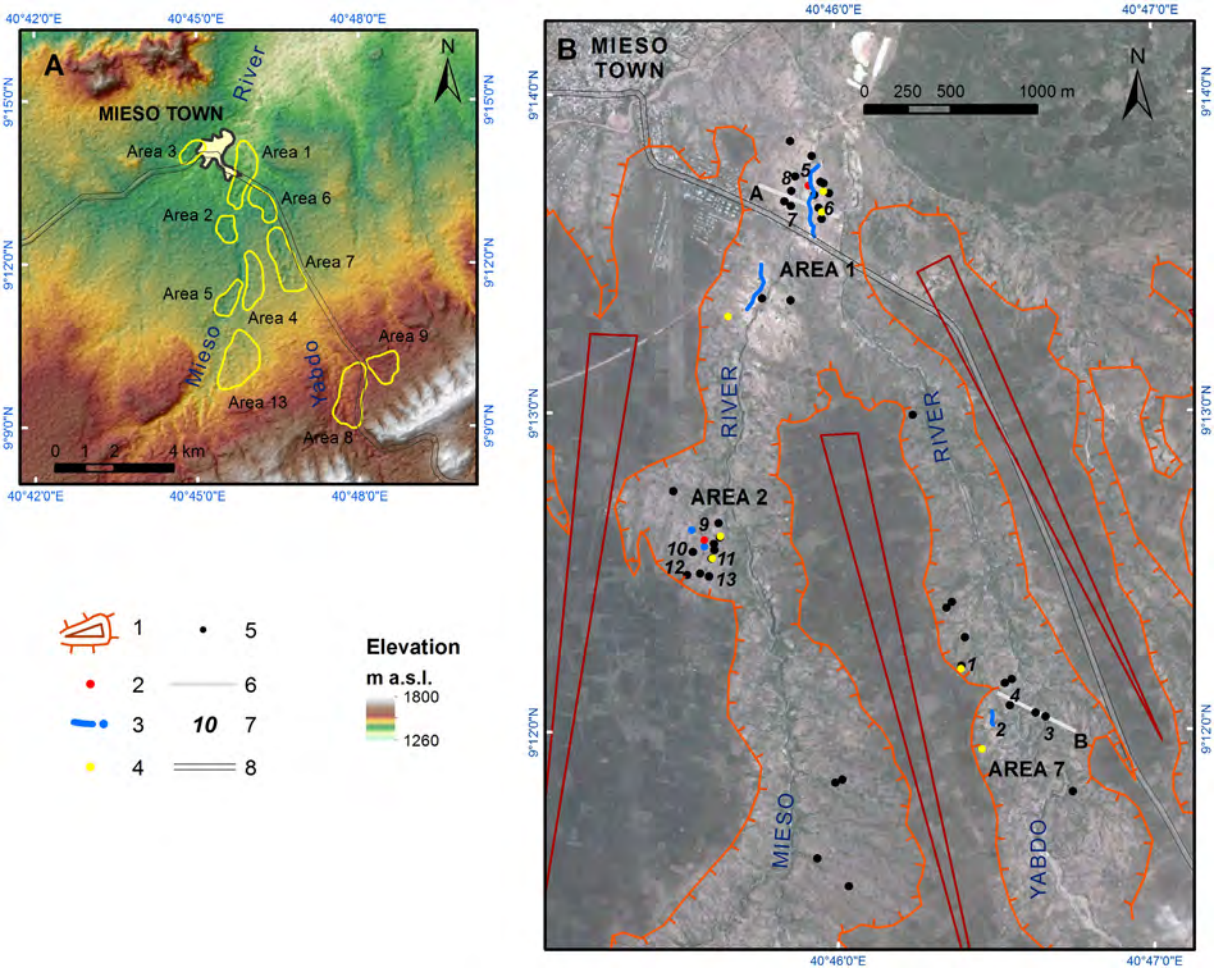

Figure 2. A) Locations of the surveyed areas. B) Mieso piedmont alluvial plain around Areas 1, 2 and 7. Legend: 1, Piedmont alluvial plain; 2, Tuff TBI exposures; 3, Tuff TA exposures; 4, Tuff CB exposures; 5, Archaeological sites; 6, Geological cross sections A (Area 1) and B (Area 2) (see Figure 3); 7, Stratigraphic logs (see Figure 3); 8, Road.

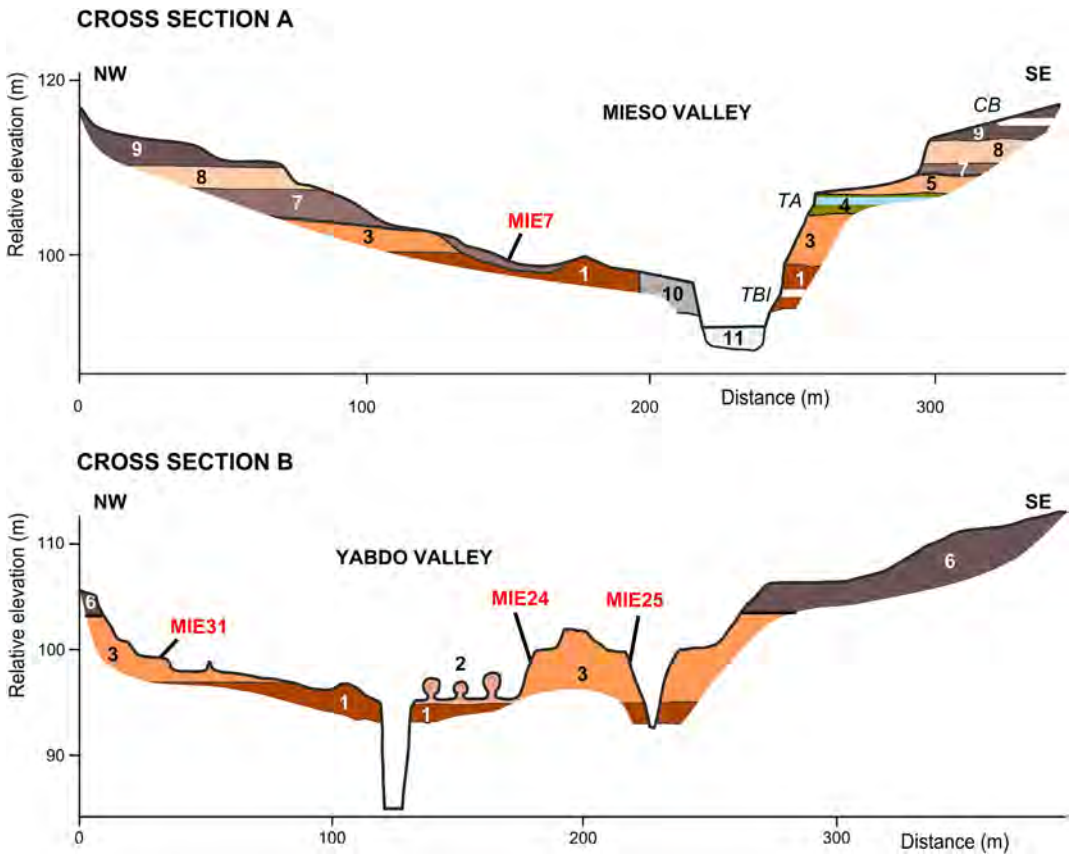

Figure 3. Geological cross sections of the Mieso and Yabdo Valleys. Legend: 1, Bed GB; 2, Stromatolitic domes in the Yabdo Valley; 3, Bed FA; 4, Bed LC; 5, Bed CD; 6, Unit II undifferentiated; 7, Bed A; 8, Bed B; 9, Bed C; 10, Fluvial terrace; 11, Bedrock. See position in Figure 2B.

(Fig. 2B). Here, the Yabdo Valley consists mainly of a gorge incised into the bedrock, while outcrops in the valley of the Mieso River reveal a 24 m thick sedimentary sequence (Fig. 3 and 4), that lies on top of welded tuffs and basalts (bedrock). The sequence is divided into two major sedimentary units (Mieso Units I and II), separated by a heavily incised disconformity. The disconformity is also demonstrated by the asymmetry of the valley downstream from the Mieso Bridge; the lower unit is exposed on the east margin, whereas on the west margin the upper unit has strongly eroded the lower unit, such that only the lowermost beds are preserved (Fig. 3 and 5A).

The lower unit (Unit I) contains a basal bed (Bed GB), composed of volcanic gravels grading laterally and vertically to fine-grained sediments (Fig. 4). The coarse sediments vary in size from granules to boulders, are subrounded to rounded, are clast-supported, and show imbricated clasts usually trending north-northeast. Nevertheless, some channels carved into the bedrock are transversal to the current Mieso course. Fine sediments contain medium and coarse sands with channel-filling structures and massive silty clays with pedogenic features, including carbonate veins. A white reworked tuff is preserved (tuff TBI) locally in a small outcrop within fine sediment deposits (Fig. 4 and 5G).

In Area 1, Bed GB contains four channel infilling episodes. Fossils are relatively common (e.g., MIE4) in this channel facies. The upper episode contains a calcrete formation at the top, defining a second lithostratigraphic unit (Bed FA). Bed FA is composed of approximately 4 m of yellow massive silty clays and sandy clays, with carbonated nodules and levels cemented by calcrete (Fig. 5C). Some of the Acheulean occurrences (MIE6 and MIE6B) derive from this bed (de la Torre et al., Accepted). These sediments include buried soils with illuvial cuttans and are light yellowish brown in colour. A palustrine bed (Bed LC) overlies these deposits. Bed LC is 2–3 m thick, and consists of a centimetric succession of laminated grey marls and clays that include calcretes at the top, followed by porous white tufas. At the top of this bed, there is a light blue volcanic ash (Tuff TA, Fig. 4 and 5A). In Area 1, Tuff TA is divided in two layers (TAi and TAs, Fig. 4 and 5E) of 15–20 cm each, separated by a tufa. The tuff is laminated locally, suggesting that it was deposited in a water body, and it is cemented by carbonates. The uppermost bed identified in Unit I (Bed CD) corresponds to a succession of silty clays, stratified in centimetric beds and cemented by calcretes, with dissolution features at the top.

In Area 1, Unit II is divided into three beds, separated by minor disconformities (Fig. 3 and 4). The lower bed (Bed A) is mainly composed of dark grey silty clay and sands, including thin layers of volcanic subrounded granules and gravels, and minor cementation. On the western margin, the archaeological site of Mieso 7 (de la Torre et al., Accepted) is included in this bed (Fig. 3), where it consists of volcanic gravels, sands and silty clays that fill an E–W palaeogully, transverse to the present Mieso River (Fig. 4 and 5A). The intermediate bed (Bed B) shows features similar to those of Bed FA, and is characterised by a sequence of light yellowish-brown massive silty clays, with calcrete formation in the middle of the bed, and a horizon of gravels. The Acheulean artefacts from the Mieso 1, Mieso 2 and Mieso 3 sites (de la Torre et al., Accepted) are located in this bed. Bed C overlies Bed B and completes the sequence documented in Area 1. Bed C begins with an erosive level of gravels that grade upwards to grey sands and dark grey massive silty clays, with argillic dark greyish-brown buried soils. Site MIE48 (de la Torre et al., Accepted) corresponds to Bed C (Fig. 4). This bed

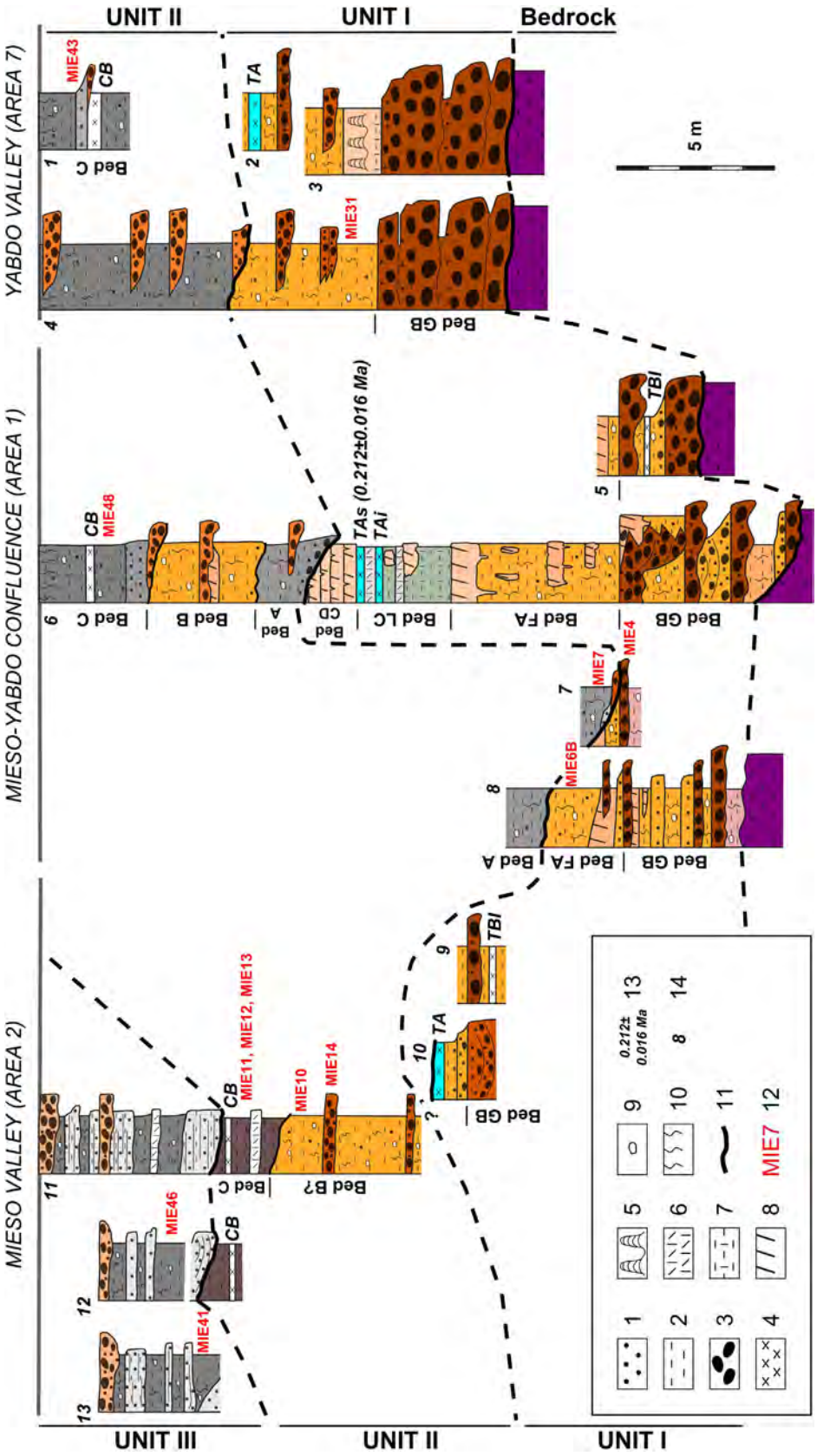

Figure 4. Stratigraphic units of the Mieso Quaternary sequence, and positions of relevant archaeo-palaeontological assemblages. Legend: 1, Sands; 2, Silty clays; 3, Gravels; 4, Tephra levels (tuffs TBI, TA and CB); 5, Domal stromatolites; 6, Tufas; 7, Marls and clays; 8, Calcretes; 9, Carbonate nodules; 10, Pedogenetic features; 11, Disconformity; 12, Archaeological sites; 13, $^{40}Ar/^{39}Ar$ age; 14, Stratigraphic log (see position in Figure 2B).

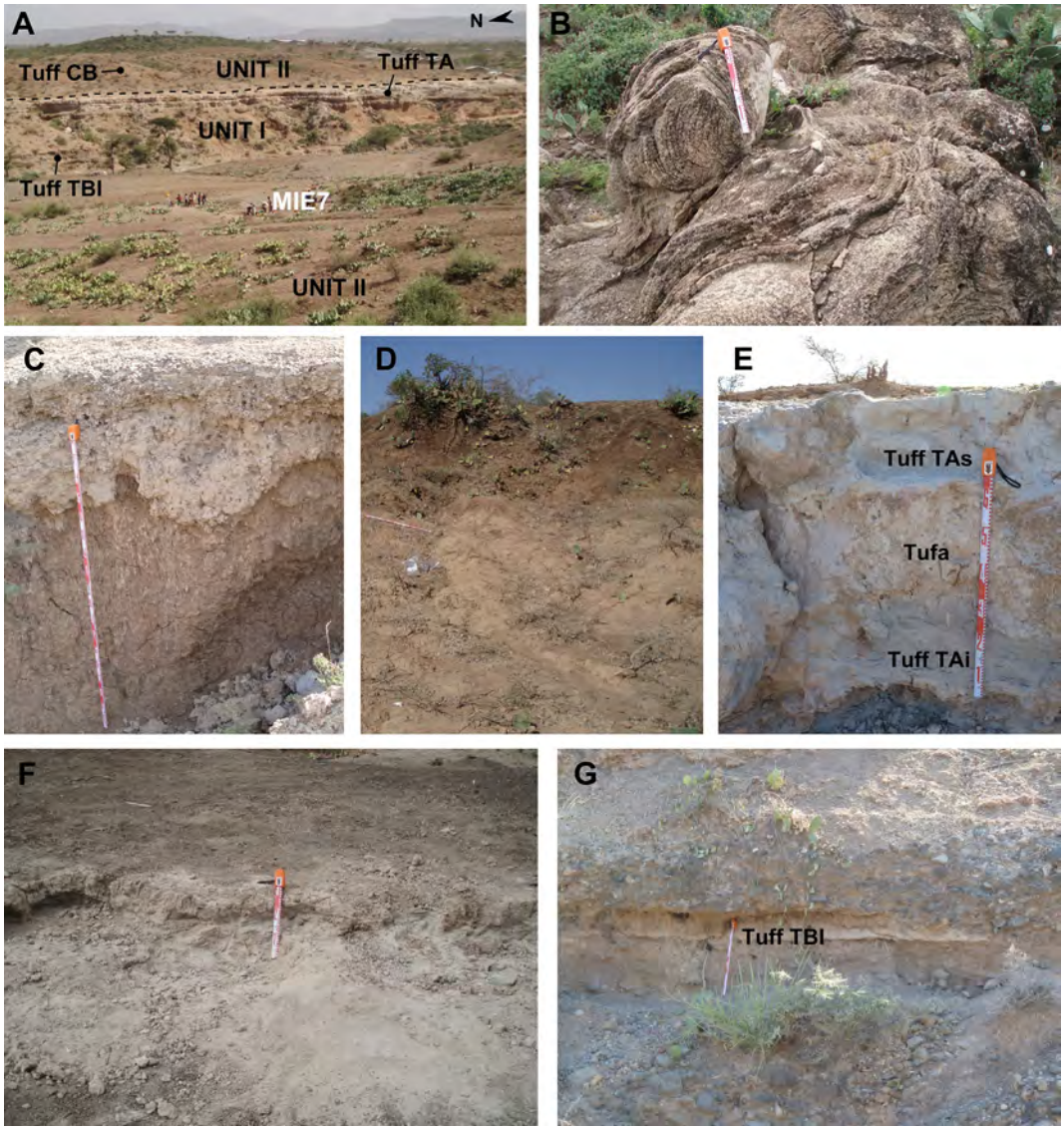

Figure 5. A) View of the Quaternary sequence downstream from the Mieso Bridge (Area 1). B) Domal stromatolites in the Yabdo Valley sequence (Area 7). C) Pedogenetic profile with calcretes in Bed FA (Unit I, Area 1). D) Unit II topsoil above reworked tuff CB (Area 7). E) Levels of tuff TA (TAi and TAs) in Area 1, separated by a tufa. F) Tuff CB exposure in Area 2. G) Bed GB (Unit I) including an exposure of tuff TBI (Area 1).

contains a third tuff level (tuff CB) that has been reworked and contaminated by detrital sediments. A dark brown soil is developed at the top of Unit II. The entire sedimentary sequence is incised by the current Mieso River, with a very recent fluvial terrace hanging 4–5 m above the present water level (Fig. 3).

Area 2 This area is situated on the western side of the Mieso Valley, 2 km upstream from the Mieso Bridge (Fig. 2B). Here, Unit I sediments on top of the volcanic bedrock are poorly exposed, making it difficult to identify different beds within the unit. The base of the unit contains 3–5 m of channelised subrounded gravels (Bed GB), showing interlayered massive silty clays where tuff TBI is partially exposed (Fig. 2B and 4). These gravel beds are followed by light yellow-brown sands and massive silty clays, possibly coeval with Bed LC of Unit 1 (Area 1), given that tuff TA is documented at the top of the sands and silty clays (Fig. 4). In Area 2, tuff TA is present as one single massive 45–55 cm thick layer, contaminated by detrital sediments. Laterally, tuff TA is unconformably beneath light yellow silty clays 4–5 m in thickness, with buried soils and thin layers of gravels. The latter contains bones and fragments of stratiform stromatolitic growths at the MIE14 locality (see de la Torre et al., Accepted). This 4–5 m sedimentary segment could be tentatively attributed to Unit II (Bed B), since it is erosive over sediments containing tuff TA and it underlies a bed that contains tuff CB (Fig. 4 and 5F). This bed containing tuff CB correlates with Bed C (Unit II), and is characterised by very dark grey clays and centimetric layers of micritic tufas with local patches of phytoclasts. Sites Mieso 11, Mieso 12, and Mieso 13 (de la Torre et al., Accepted) are located in these deposits. Tuff CB is well preserved at the top of Bed C, and consists of a white layer of fallout ashes 5–10 cm in thickness.

Unit III lies on top of Unit II (Fig. 4). This new unit, unreported in Area 1, is composed mostly of light grey sandy layers with laminations and cross-stratifications, massive silty clays with carbonate nodules and pedogenic features, and gravel beds. Unit III also contains patches of tufas within the silty clays beds, and preserves stratified LSA assemblages such as Mieso 41 and Mieso 46.

Area 7 This area is located along the margins of the Yabdo Valley (Figure 2B), 3 km upstream from the confluence with the Mieso

River (Area 1). In Area 7, the Yabdo Valley shows open morphology in the upper slopes where incision of the sedimentary sequence commences, and a narrow gully (approximately 3 m wide and 9–10 m deep) in the lower section of the valley (Fig. 3), where the Yabdo River dissects the welded tuffs and basalts of the bedrock.

The base of the siliciclastic sequence lies at 8 m above the present stream bed of the Yabdo River (Fig. 3). It consists of a 4 m thick segment with fining-upward beds of subrounded gravels, moderate and poorly sorted, interbedded with sand and silty clay layers towards the top. These sediments presumably correspond to basal bed GB (Unit I) from Area 1. Fine-grained sediments (Bed FA) overlie Bed GB, and are characterised by overbank light yellow silty clays, sands and centimetric layers of gravels, interpreted as channel infillings. The MIE 31 archaeological site (de la Torre et al., Accepted) is located on the west of the Yabdo Valley, and is included within a mud layer near the base of the bed (Fig. 3 and 4), which is cut by a channel with an overall N–S direction. On the east margin of the Yabdo Valley, the base of Bed FA is represented by a level of marls, over which three stromatolitic domal structures formed (Fig. 3 and 5B). These sediments overlying Bed GB would presumably correlate with Bed FA and Bed FC, as defined in Area 1, given that eroded remnants of tuff TA are identified at the top of this sequence on the west margin of the valley. In Area 7, tuff TA, massive, fractured, and partially weathered, crops out as a 40 cm thick unit. Where reworked by aeolian processes, tuff TA is 40–60 cm thick and partially laminated.

Above tuff TA, an unconformity identified on the western margin of the valley leads to Unit II. In Area 7, Unit II consists of an undifferentiated succession of dark grey fine sediments, including several gravel channels. Tuff CB is documented near the top of this sequence at the MIE43 locality (Fig. 4 and 5D). Here, tuff CB consists of a 10–15 cm white ash layer that is laterally reworked by aeolian processes. An illuvial dark brown soil affected by ploughing activities caps the sequence in this area (Fig. 5D).

Depositional environments

The Mieso sedimentary deposits correspond to an alluvial sequence related to the development of a regional low gradient alluvial plain formed in generally semi-arid conditions. High-energy hydrodynamic flows are typical of the base of Unit I (Bed GB). In this unit, at least four aggradation phases exist, and are mainly composed of channels of conglomerates and (to a lesser degree) overbank deposits, usually corresponding to fining-upward cycles. Basal channels often fill scours carved in the volcanic bedrock, and have directions parallel and transverse to the modern fluvial courses. The lowermost layer of volcanic tuff is locally preserved in the overbank deposits (tuff TBI, Fig. 5G). These deposits are overlain by lower energy alluvial deposits (Bed FA), in which fine-grained sediments dominate. These sediments include buried illuvial light yellowish brown soils and calcretes (Fig. 5C), suggesting a semi-arid environment controlled by seasonal and local soil moisture fluctuations (Schaetzl and Anderson, 2006). Domal stromatolites from Bed FA indicate the presence of shallow pools or wetlands across the alluvial plain (Fig. 5B). Similar conditions are also observed in Bed LC, where a succession of laminated clays, marls and tufas indicates a palustrine environment near Mieso town (Area 1). Tuff TA was deposited during the formation of Bed LC. When in alluvial sediments, tuff TA is preserved as a single massive layer. However, in Bed LC tuff TA contains two layers (TAi and TAs), separated by a thin tufa (Fig. 5E). After Bed LC, drier conditions prevailed in Area 1, as shown by thin mud layers indurated by calcretes (Bed CD), with dissolution features at the top.

Low-energy sedimentation dominates the alluvial deposits of Unit II. This unit features dark greyish-brown soils, which could potentially indicate wetter conditions and an increase in the vegetation cover. Nevertheless, more semi-arid environments prevail in Bed B, where sedimentological features are more similar to those of Unit I (Bed FA). The infilling direction follows the regional S–N gradient, although transverse directions exist due to local topography (e.g., volcanic features). The alluvial plain of Unit II contains local wetland areas, as suggested by stratiform stromatolites, dark silty clays and tufas. Tuff CB, deposited near the top of Unit II, is better preserved in the palustrine environment of Area 2 (Fig. 5F), whereas in Areas 1 and 7 it appears to be reworked by aeolian and alluvial processes (Fig. 5D).

The Mieso piedmont alluvial plain was formed mainly at the top of Unit II, where an illuvial dark brown soil had developed (Fig. 5D). On top of Bed II, a more recent unit is observed in Area 2 (Unit III). This fluvial unit is dominated by sandy channels and overbank deposits, where patches of tufas indicate the former presence of palustrine local pools.

Archaeology

The density of finds is uneven across the Mieso Valley, with some localities yielding clusters of fossils and artefacts, while others were named on the basis of low density scatters. A total of 37.3% of the localities documented by de la Torre et al. (Accepted) are stratigraphically positioned in Unit I at the bottom of the sequence, and the same frequency ($n = 19$) is found in the overlying Unit II. A total of five localities (9.8%) are attributed to Unit III, in the upper part of the sedimentary sequence (see Fig. 4). Within Unit I, most of the finds are within Bed FA, while in Unit II they are more widely distributed across Beds B, C and, to a lesser extent, in Bed A (see facies descriptions above). In Unit III, all identifiable localities are positioned in Bed IF.

A total of 80.4% of the 51 localities listed by de la Torre et al. (Accepted) contained stone tools, while 62.7% yielded fossils. There seems to be preferential preservation of fossils in the Mieso River area, where 72.2% of localities yielded bones, in contrast to the Yabdo sequence, in which only 40% of localities contained fossils. All Unit III sites yielded fossils, whilst bones were documented in 68.4% and 57.9% of Unit II and Unit I localities, respectively.

Several of the Area 2 sites from Unit III Bed IF show LSA technology, characterised by obsidian bladelet production. In the upper course of the Yabdo River (see Fig. 2), some localities could potentially be attributed to the MSA, as suggested by the predominance of basalt cores and flakes and the absence of handaxes, although further characterisation of such assemblages is required.

The stratigraphy, depositional environments and chronology of the Mieso localities that can confidently be attributed to the Acheulean on the basis of the presence of handaxes and/or other large cutting tools are the focus of this paper, while their archaeological contexts are discussed at length by de la Torre et al. (Accepted). The main Acheulean localities are found in Area 1 (Mieso 4–7 and Mieso 48), which correspond to the middle course of the Mieso River, and in Area 7 (Mieso 31), on the left bank of the Yabdo River and around 3 km from the confluence with the Mieso River (see Fig. 3).

All of the Acheulean assemblages reported in the Mieso Valley are included in the alluvial deposits of the Mieso and Yabdo Rivers. Area 1 archaeological localities are associated with layers of silty clays, sands and gravels, and include a relevant stratified assemblage in Unit II Bed A, Mieso 7, where handaxes are found in primary context on top of a clay unit (see details in de la Torre et al., Accepted). The site of Mieso 31 is at a lower stratigraphic position, located in Unit I Bed FA in Area 7. This Acheulean site corresponds to a cyclic alluvial aggradation sequence with gravels, sands and silty clays, with most of the artefacts associated with the silty

clay unit. The high frequency of refitted artefacts and lack of preferential orientations suggest a gentle depositional environment in which most of the Mieso 31 assemblage is preserved in primary position (see discussion by de la Torre et al., Accepted).

Chronology of the Mieso beds

To establish a chronological framework for the Mieso sedimentary and archaeological sequences, several tuff samples were collected for tephrochemistry and $^{40}Ar/^{39}Ar$ dating. Tuff TBI was sampled in Areas 1 and 2, and tuffs TA and CB in Areas 1, 2 and 7.

Tephrochemistry Three samples that were prepared for EPMA (Electron Probe Microanalysis) contained fresh glass: MP-TBI (tuff TBI, Area 1), M31-TA (tuff TA, Area 7) and M14-CB (tuff CB, Area 2). Samples M14-CB and MP-TBI contained rhyolitic glass, while sample M31-TA glass was dacitic (see Fig. 6). M31-TA glass covers a wide compositional range, with two broad populations differing in Ca, Al, Mg, and Si concentrations. The three samples are clearly distinguishable from each other in most elements. The EPMA results are presented in Table 1.

These glass compositions were compared with published glass compositions for other similarly aged tuffs in this region of Ethiopia. Since we do not have access to samples of these regional tuffs, we were not able to analyse them independently (following our own methods), which could affect the quality of our comparison because of inter-lab differences in EPMA methods. A comparison to the EPMA -derived major and minor element data for the Dahuli (Busidima; Quade et al., 2008), Bironita (Geraads, 2004; Wynn et al., 2008), Waidedo Vitric Tuff (WAVT), Upper Herto Member at Bouri (Clark et al., 2003) and Busidima (Wynn et al., 2008), and partial analysis of Middle Awash tuffs (Clark et al., 1994), reveals that none is a perfect match. However, the tuff TBI glass matches the composition of the Dahuli well in all non-volatile elements other than Fe_2O_3, and both are still low in Fe_2O_3 compared with the other tuffs considered. The CB tuff is considerably higher in Al_2O_3 compared with all others considered. The tuff TA sample has higher Fe_2O_3, MnO, and TiO_2 glass than any of the samples in the comparison.

Tephrochronology In general, tufaceous deposits in the region show reworking features. Samples for $^{40}Ar/^{39}Ar$ dating were collected in the fresher and undisturbed outcrops, which are located in the palustrine deposits of Area 1 (tuff TA), Area 2 (tuff CB), and limited patches of tuff TB in Area 7. From these areas, only three samples with potentially significant Pleistocene single-grain age populations were identified. One of these three samples belongs to tuff TA (MP-TASUP-1), and two samples belong to tuff CB (M43-CB and M43-CB-1). All three were analysed in detail in an effort to discern the presence of a juvenile population that could potentially be ascribed to an eruption age (Fig. 7). All samples are presented as probability density functions with the associated age-ordered number of analyses, K/Ca ratios and abundance of radiogenic argon ($^{40}Ar^*$). After rejection of samples with low radiogenic

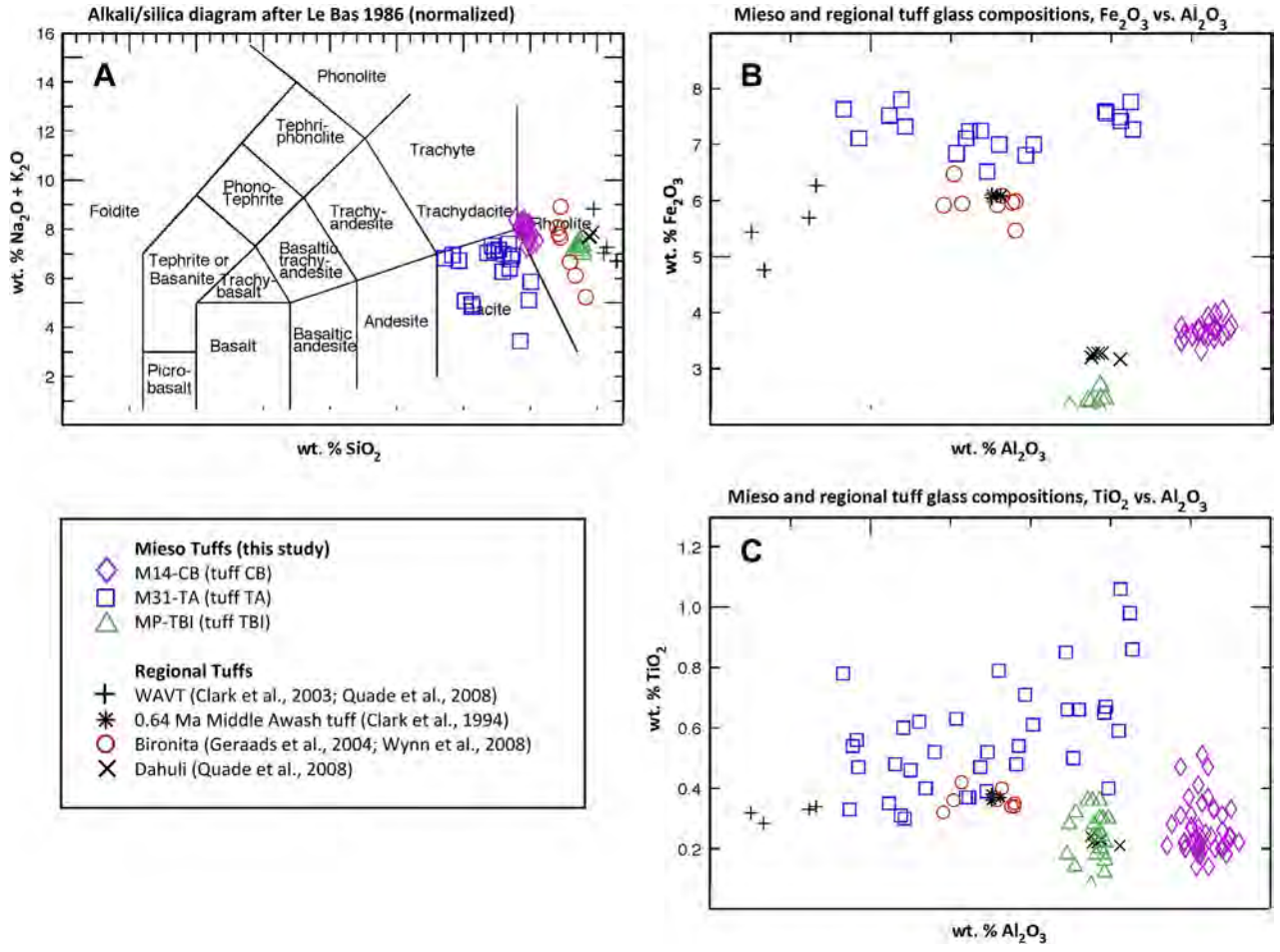

Figure 6. Glass composition for Mieso tuffs, compared to regional marker tuffs. A) Alkali-silica diagram, after Le Bas et al. (1986). Tuff CB is a low-silica rhyolite, TBI is rhyolitic, and TA is variable but mainly dacitic. B and C) Glass compositions, Fe_2O_3 and TiO_2 vs. Al_2O_3. Tuff CB has higher Al_2O_3 than the comparative samples, and TA has a broad compositional range. Tuff TBI has a similar composition to the Dahuli tuff, with slightly lower Fe_2O_3 but comparable concentrations of the other non-volatile elements, including TiO_2. Data for comparative tuff compositions from Clark et al. (1994, 2003), Geraads et al. (2004), Quade et al. (2008), and Wynn et al. (2008).

Table 1
EPMA results for glass from samples MP-TBI (tuff TBI, Area 1), M31-TA (tuff TA, Area 7) and M14-CB (tuff CB, Area 2).

Sample	*n*	SiO_2	TiO_2	Al_2O_3	Fe_2O_3	MnO	MgO	CaO	Na_2O	K_2O	Sum
M14-CB	45	68.34	0.27	14.16	3.66	0.11	0.06	0.97	3.85	3.90	94.95
StDev		1.13	0.09	0.21	0.16	0.03	0.02	0.05	0.62	0.14	1.53
M31-TA (1)	25	67.95	0.50	10.81	7.07	0.31	0.04	0.60	2.48	3.94	92.99
StDev		1.14	0.14	0.75	0.32	0.05	0.03	0.15	1.17	0.32	1.69
M31-TA (2)	11	64.70	0.72	12.87	7.38	0.35	0.23	1.32	3.04	3.23	93.11
StDev		0.63	0.20	0.31	0.25	0.06	0.08	0.13	1.19	0.21	1.68
MP-TBI	30	70.76	0.24	12.78	2.48	0.08	0.11	0.79	2.80	4.39	94.18
StDev		1.47	0.08	0.72	0.41	0.04	0.04	0.17	0.63	0.39	1.29

Sample M31-TA glass is subdivided into two populations based on subtle compositional differences.

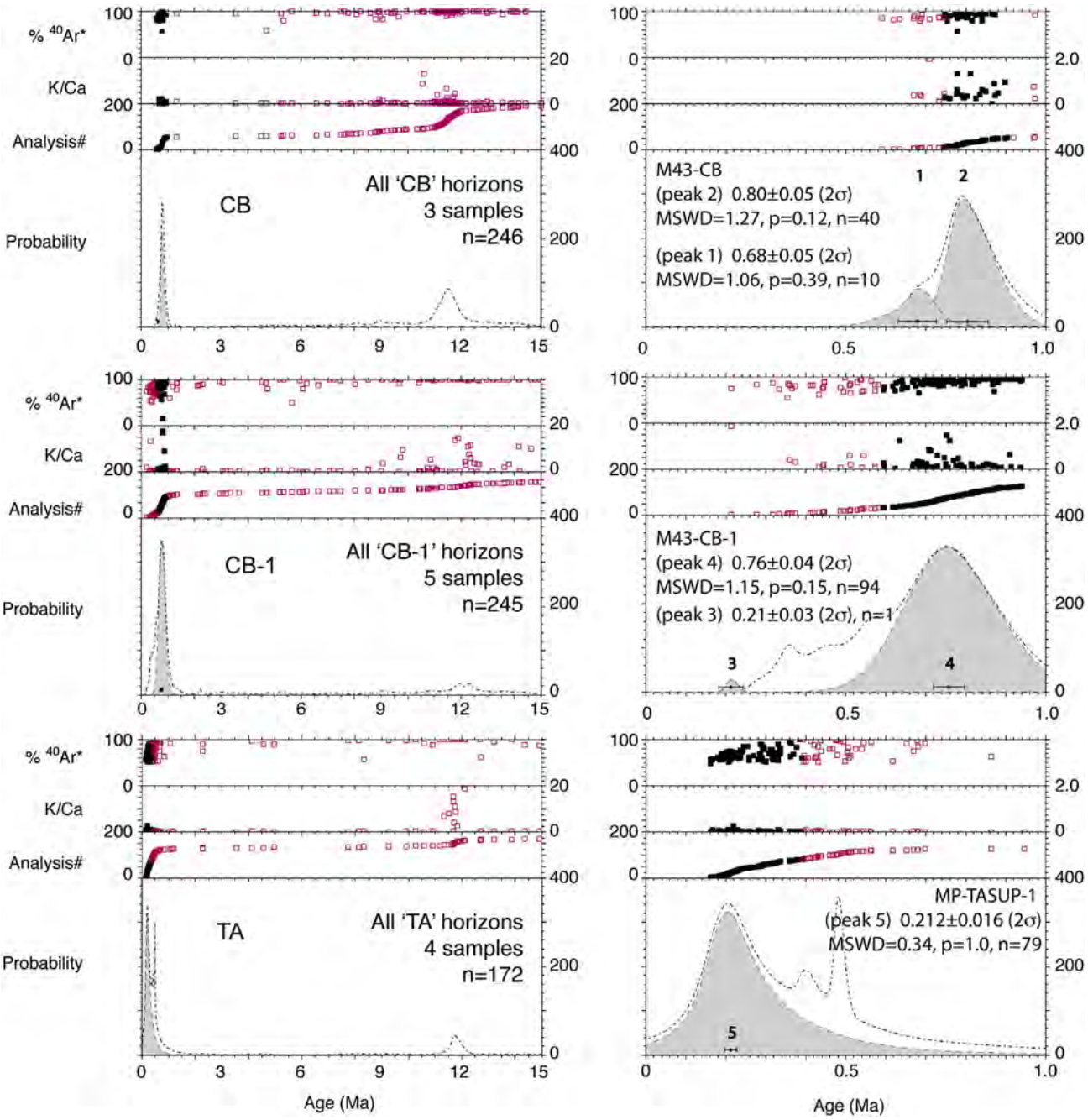

Figure 7. Probability density functions (PDF) for $^{40}Ar/^{39}Ar$ age data from single feldspar grains in Mieso tuffaceous samples. Dashed curve gives the PDF for the entire data set. The grey area under the solid curve gives the best-fit Gaussian distributed age population in the Pleistocene age range. Three panels to the left show a compilation of all samples from a given horizon (CB and TA). Right-hand panels show data from three selected samples from each of these three horizons that have resolvable 'young', i.e., Pleistocene, age populations. For these samples, the error-weighted mean and standard error of the weighted mean are given at the 2σ (two sigma uncertainty) confidence level for the observed Gaussian distributed populations. Age populations are identified as numbered peaks (1–5). Peak 5, from samples M43-CB-1 contains only one grain age and serves only to illustrate the data for this youngest grain for comparison with the overlying deposits.

yields (<50% $^{40}Ar^{*}$) and assuming normally distributed data, each sample population was screened to obtain the best Gaussian fit to the calculated grain ages.

All samples showed a broad range of single-grain ages spanning mid-Miocene to Pleistocene. Peaks were observed at ca. 11.5 Ma (millions of years ago), 9.0 Ma, and a cluster at <1.0 Ma (Fig. 7). These ages are consistent with the regional geology, where rifting of the northern section of the MER commenced at ca. 11 Ma and continues today (Ukstins et al., 2002; Wolfenden et al., 2004, 2005). Notably, the prominent ~11.5 Ma age peak seen in much of the Mieso section is consistent with $^{40}Ar/^{39}Ar$ ages ranging from 10.9 to 11.7 Ma obtained for silicic volcanic rocks, including ignimbrites, that crop out approximately 100 km to the west of the field area, along the western side of the MER near Ankober (Ukstins et al., 2002). Pleistocene ages are consistent with the recent and ongoing volcanism of the region (Kidane et al., 2010; Field et al., 2013).

Tuff CB: The samples of this tuff were obtained from Unit II (Area 7). In the first sample (M43-CB), a total of 225 individual grains were analysed. The majority of analyses had K/Ca ratios <1.0 and generally close to 0.1, indicating a population dominated by plagioclase feldspar. The best-fit age population (Fig. 7, 'peak 4') of 94 single grains yields an age of 0.76 ± 0.04 Ma (2σ, two sigma uncertainty) with acceptable statistical criteria (MSWD = 1.15, Probability = 0.15, n = 94 of 225). The data are skewed toward younger ages with an apparent minimum close to 0.21 ± 0.03 Ma (2σ) ('peak' 5). A second sample (M43-CB-1) yields a best-fit age population ('peak 2') of single grains at 0.80 ± 0.05 Ma (2σ) with acceptable statistical criteria (MSWD = 1.27, Probability = 0.12, n = 40 of 225), but indistinguishable from the M43-CB 'peak 4'. A subordinate and younger peak is apparent at 0.68 ± 0.05 (2σ) (MSWD = 1.06, Probability = 0.39, n = 10 of 225).

Tuff TA: Obtained from the upper horizon of the LC bed in Unit 1, the sample MP-TASUP (tuff TAs, Area 1) is also dominated by plagioclase with K/Ca ratios <1.0. A best-fit age population (Fig. 7, 'peak 3') of 79 single grains yields an age of 0.212 ± 0.016 Ma (2σ) with acceptable statistical criteria (MSWD = 0.34, Probability = 1.00, n = 79 of 226). This age is indistinguishable from the minimum age observed in the skewed distribution of ages seen in the TB sample.

During the sample preparation stage, it was noted that some of the Mieso samples contained minor amounts of quartz, some grains of which appeared to be well-rounded, suggesting reworking of sediments. The single crystal populations in the Mieso samples are characterised by broad age distributions spanning more than 10 Ma and appear to contain grains coeval with the initiation of rifting in the region. The main age populations in the CB samples (Fig. 7, 'peaks 2, 3 and 4') do not conform to the stratigraphic sequence, i.e., the main age population for the TA sample at 0.212 ± 0.016 Ma, which is overlain by the CB sample that has older populations of 0.80 ± 0.05 Ma and 0.68 ± 0.05 Ma. In the Pleistocene age range, sample CB shows a skew in the single-grain age distribution that has a minimum value, ca. 0.2 Ma, similar to the age distribution seen in sample TA. Taken together, these observations demonstrate significant amounts of xenocrystic contamination for tuff CB, due to partial reworking (Area 7). Therefore, a simple interpretation is that the ages defined by the single-grain populations serve as upper limits to the age of deposition of the strata in the basin. In this case, sample TA provides the best numeric estimate at 0.212 ± 0.016 Ma for the upper limit of Mieso Unit I.

Discussion

The Mieso sequence is composed of weakly consolidated alluvial sediments including palustrine patches, divided into three units (I, II and III) bounded by disconformities (Fig. 3 and 4). The older units (I and II) contain archaeological remains corresponding to the Acheulean (de la Torre et al., Accepted). Several levels of spatially limited, fine-grained volcanic tuffs were recognised interlayered in Units I and II. These were located at the base of Unit I (tuff TBI), near the top of Unit I (tuff TAi and TAs), and towards the top of Unit II (tuff CB).

Within Unit I, tuff TBI did not provide suitable material for $^{40}Ar/^{39}Ar$ dating, while tuff TAs yielded an age of 0.212 ± 0.016 Ma for the top of this unit (Fig. 7). The dated tuff sample derives from a palustrine area where reworking processes are limited (Fig. 4 and 5E), and the age obtained is statistically consistent. With multiple age peaks around 0.80 Ma, 0.68 and 0.21 Ma, the data obtained for tuff CB in Area 7 suggest xenocrystic contamination. Since Unit II incises significantly into Unit I, tuff CB xenocrystic populations could contain material both from tuff TA and previous volcanic events (0.68 and 0.80 Ma xenocrysts). However, glass composition for tuff CB in Area 2 (sample M14-CB) is internally similar (no outliers in a population of 45 glass shards analysed), and differs from those of tuffs TA and TBI, providing a limit for the degree of contamination. It should be noted that the tuff CB sample analysed by EPMA (M14-CB) came from Area 2, while the sample dated using the $^{40}Ar/^{39}Ar$ method came from Area 7, indicating that tuff CB is more heavily contaminated by older detritus in Area 7 compared with Area 2. In the Mieso study area, the only previous volcanic event observed in the sedimentary sequence corresponds to tuff TBI, which could be the origin of the 0.68 or 0.80 Ma xenocrysts. This tentative correlation situates the base of Unit I near the Early-Middle Pleistocene, although no radiometric ages are yet available for the deposition of tuff TBI. In summary, reliable dating of tuff TAs at 0.212 ± 0.016 Ma, together with the peak at 0.210 Ma from tuff CB (Fig. 7), strongly suggest that the top of Unit I, and probably the bottom of Unit II, correspond to the late Middle Pleistocene. The presence of hand-axe bearing assemblages in both units reveals that Acheulean technology younger than 0.212 Ma persisted in the Mieso area. Given that in this time interval there is evidence of MSA technology in nearby sequences such as Gademotta (Morgan and Renne, 2008; Sahle et al., 2014) and elsewhere in the region (see review by McBrearty and Brooks, 2000), this late age for the Mieso Acheulean has relevant implications for the timing of the transition to the MSA in East Africa (see discussion by de la Torre et al., Accepted).

Although biostratigraphic and archaeological correlations with other sequences in the eastern basin of the Afar Depression are yet to be developed, the chronostratigraphic setting of Mieso in its regional context can be discussed on the basis of the available data. In the Middle Awash area, the upper part of the Bouri Formation is divided into the Dakanihylo and Herto Members (Clark et al., 2003; WoldeGabriel, 2012). The Dakanihylo Member contains 1.00–0.26 Ma sandstones where Acheulean stone tools are reported. Thus, Mieso Unit I (>0.212 Ma) could potentially overlap with the Dakanihylo Member. On the other hand, Mieso Unit II (<0.212 Ma) could correlate mainly with the Herto Member (fluvial and lacustrine sediments) dated to between 0.260 and 0.160 Ma (Clark et al., 2003), which yields Acheulean and MSA stone tools associated with early anatomically modern humans (White et al., 2003).

Similar chronostratigraphic units are also reported in the Gona, Dikika, and Hadar regions (central western basin floor of the Afar Depression). In these areas, the Busidima Formation preserves fluvial systems (Quade et al., 2008; Wynn et al., 2008; Campisano, 2012), where the upper parts contain less mature coarse sediments and mainly fine sediments with thick palaeosols (Quade et al., 2008). These upper deposits are interpreted as eastward flows coming from the escarpment that gave way to an alluvial-fan plain,

similar to the sedimentary settings from Mieso Units I and II. In Gona, the lower boundary of the upper Busidima Formation is the Dahuli Tuff, $^{40}Ar/^{39}Ar$ dated at 0.81 Ma (Quade et al., 2004, 2008), which is in agreement with the age of xenocrysts from Mieso tuff CB (potentially derived from the tuff TBI volcanic event). In a preliminary comparison, tuff TBI glass matches the composition of the Dahuli in all non-volatile elements other than Fe_2O_3, and both are low in Fe_2O_3 compared with the other tuffs considered.

The top of the Busidima Formation contains the Korina Tuff (Wynn et al., 2008) and the Waidedo Tuff, dated at 0.16 Ma (Clark et al., 2003; Quade et al., 2008). This places the top of the Busidima Formation at a younger age than the tuff TAs at Mieso Unit I. Although no radiometric dates are yet available for the top of Mieso Unit II, the upper part of this unit shows similarities with the top of the Busidima Formation, since both are characterised by the development of illuvial dark brown topsoils before the fluvial incision. Nevertheless, compositional differences between tuff CB and Waidedo tuff do not support a direct correlation (Fig. 6). In addition, the presence of a high relief discontinuity between Mieso Unit I and Unit II suggests a significant hiatus between these two units, which could place most of Unit II within the Late Pleistocene.

Another sequence potentially equivalent to the Mieso Middle Pleistocene units is at Arba (northern MER, Clark and Williams, 1978), to the south-west. In this area, Late Acheulean surface artefacts were reported in a gravelly alluvial plain (Clark and Williams, 1978). This facies could be related to the south-west extension of the Mieso alluvial piedmont that could have been formed during a second pedimentation phase as identified in the SE margin (Coltorti et al., 2011a, b). A minimum age for this pediment is provided by the Berak stratigraphic unit, dated at 35,080 ± 280 years BP (Abebe and Coltorti, 2011). This unit covers the pediment and is terraced at +10 m in the adjacent rift floor. The Berak unit is incised by the Adakaloya unit that contains tufas dated between 16,810 ± 100 and 6200 ± 40 years BP (Abebe and Coltorti, 2011).

Similar chronostratigraphic units are also reported in the Aladi Springs site. This site, approximately 26 km to the NE of Mieso, contains an MSA industry under a brown gritty clay (Clark and Williams, 1978), and upper tufa layers with LSA stone tools dated at 11,070 ± 160 years BP (Williams et al., 1977; Clark and Williams, 1978). These upper layers provide a comparative age for the third unit located in Mieso (Unit III). In the Mieso Valley, Unit III caps Unit II and contains LSA occurrences (de la Torre et al., Accepted), probably associated with wetter climatic conditions at some point in the Late Pleistocene, as suggested by the widespread presence of tufa deposits (Clark and Williams, 1978; Abebe and Coltorti, 2011). The last sedimentary episode identified in the Mieso area corresponds to a fluvial terrace at 4–5 m over the Mieso River that was probably deposited during the Holocene.

Conclusion

The Quaternary sequence of Mieso is related to the formation of a low gradient piedmont alluvial plain in the southern Afar Depression (Ethiopia), along the foothills of the SE Escarpment. The Mieso piedmont alluvial plain is currently positioned at 25 m above the modern Mieso and Yabdo Rivers, whose incision has exposed an alluvial sequence over weathered volcanic bedrock.

The geological study of this sequence across the better exposed outcrops has enabled us to define three stratigraphic units separated by disconformities. The lower unit (Mieso Unit I) contains a gravel lower bed, and upper beds where fine sediments with pedogenic features (calcretes and argillic yellow brown soils) dominate. Mieso Unit II is represented mainly by silty clays and sands, and small gravel channels. Fine sediments preserve usually argillic dark brown soils, especially near the top of the unit, where the piedmont alluvial surface preserves thicker soil. Units I and II both preserve surface and stratified Acheulean assemblages (de la Torre et al., Accepted), while a third fluvial unit (Mieso Unit III) contains LSA occurrences. Throughout the deposition of these three units, small palustrine settings dotted the alluvial landscape, as indicated by tufas, stromatolites, clays and marls.

Three tephra layers are documented, interbedded between Units I and II. These layers are positioned at the base of Unit I (tuff TBI), towards the top of Unit I (tuff TA), and near the top of Unit II (tuff CB). Tuffs are exposed discontinuously, having been eroded and partially reworked in alluvial settings. Argon/argon dating provided a consistent age for the top of tuff TA, preserved in a palustrine environment. This date positions the top of Unit I at 0.212 ± 0.016 Ma. Dates for tuff CB show multiple age populations tentatively associated with xenocrystic contamination processes, with a peak around 0.21 Ma, and older peaks around 0.80 Ma (potentially related to reworking of the lowermost tuff, TBI). Radiometric results and comparison of the Mieso sedimentary deposits to nearby sequences in the Afar region, position Mieso Unit I in the Middle Pleistocene, and Mieso Unit II in the late Middle Pleistocene, and probably within the Late Pleistocene. Both units contain Acheulean assemblages, and the date of 0.212 ± 0.016 Ma for tuff TA ranks the Mieso handaxe-bearing assemblages among the most recent occurrences of Acheulean technology in East Africa (de la Torre et al., Accepted). The Mieso Unit III was deposited in the Late Pleistocene and probably also during the Holocene, as evidenced by the LSA assemblages and stratigraphic correlations with nearby sequences situated at the foothills of the SE margin.

While the analysis of the LSA sequence of Mieso is still in progress, the study of the Acheulean-bearing deposits (de la Torre et al., Accepted) reveals sparse archaeological occurrences that are characterised by low density lithic assemblages where lava artefacts including cleavers and bifaces predominate. Stone assemblage compositions of Mieso sites indicate heavily fragmented reduction sequences, which are interpreted as the result of highly mobile transport patterns (de la Torre et al., Accepted). Such features provide a characteristic pattern for the late Acheulean at Mieso, for which this paper has provided a chronostratigraphic framework.

In summary, the previously-unreported deposits in the Mieso area, which include Middle and Upper Pleistocene deposits with stratified archaeological assemblages, constitute a relevant new sedimentary sequence that contributes to expanding our knowledge of Pleistocene environments, and permits us to gain a better understanding of human behavioural variability in East Africa during the Late Quaternary.

Acknowledgements

We thank the Authority for Research and Conservation of Cultural Heritage of the Ministry of Culture and Tourism, and the Ministry of Mines, Ethiopia, for field and sampling permits. We are also thankful to Solomon Kebede, Dawit Tibebu, Adrián Arroyo, Jorge Martínez-Moreno and Rafael Mora for their assistance and support during the fieldwork. $^{40}Ar/^{39}Ar$ samples were prepared by Leticia Miguéns Rodríguez (Sample Preparation Laboratory, CENIEH). $^{40}Ar/^{39}Ar$ dating was conducted in the NERC Argon Isotope Facility. We thank Giday WoldeGabriel and the JHE reviewers for their comments on earlier versions of this paper. Fieldwork in Mieso was funded by the Direccion General de Bellas Artes (Ministry of Culture, Spain), and the British Academy (SG-54216). $^{40}Ar/^{39}Ar$ dating was funded by a NIGFSC grant (IP-1243-0511).

References

Abebe, B., Coltorti, M., 2011. The southern border of the Afar. In: Acocella, V., Abebe, B., Coltorti, M. (Eds.), Excursion Guide: Tectonic Landforms and Volcanism in the Southern Afar. Presented at the IAG Regional Conference 2011, International Association of Geomorphologists. Ethiopian Association of Geomorphologists, Addis Ababa, Ethiopia, pp. 9–26.

Abebe, B., Coltorti, M., Pizzi, A., 2005. Rates of Late Quaternary deformation along the Wonji fault belt in the Lakes Region, Main Ethiopian Rift. Rendiconti della Società Geologica Italiana 1, 41–43.

Abebe, B., Acocella, V., Korme, T., Ayalew, D., 2007. Quaternary faulting and volcanism in the Main Ethiopian Rift. J. Afr. Earth Sci. 48, 115–124.

Berhe, S.M., 1986. Geologic and geochronologic constraints on the evolution of the Red Sea-Gulf of Aden and Afar Depression. J. Afr. Earth Sci. 5, 101–117.

Beyene, A., Abdelsalam, M.G., 2005. Tectonics of the Afar Depression: A review and synthesis. J. Afr. Earth Sci. 41, 41–59.

Campisano, C.J., 2012. Geological summary of the Busidima Formation (Plio-Pleistocene) at the Hadar paleoanthropological site, Afar Depression, Ethiopia. J. Hum. Evol. 62, 338–352.

Chernet, T., Hart, W.K., Aronson, J.L., Walter, R.C., 1998. New age constraints on the timing of volcanism and tectonism in the northern Main Ethiopian Rift–southern Afar transition zone (Ethiopia). J. Volcanol. Geoth. Res. 80, 267–280.

Clark, J.D., Williams, M.A.J., 1978. Recent archaeological research in southeastern Ethiopia. 1974-1975. Annales d'Ethiopie 11, 19–44.

Clark, J., De Heinzelin, J., Schick, K., Hart, W., White, T., WoldeGabriel, G., Walter, R., Suwa, G., Asfaw, B., Vrba, E., Haile-Selassie, Y., 1994. African *Homo erectus*: old radiometric ages and young Oldowan assemblages in the Middle Awash Valley, Ethiopia. Science 264, 1907–1910.

Clark, J.D., Beyene, Y., WoldeGabriel, G., Hart, W.K., Renne, P.R., Gilbert, H., Defieur, A., Suwa, G., Katoh, S., Ludwig, K.R., Boisserie, J.-R., Asfaw, B., White, T.D., 2003. Stratigraphic, chronological and behavioural contexts of Pleistocene *Homo sapiens* from Middle Awash, Ethiopia. Nature 423, 747–752.

Coltorti, M., Pizzi, A., Abebe, B., Disperati, L., Firuzabadi, D., Pomposo, G., Pontarelli, L., Sacchi, G., Salvini, R., 2011a. Geology and tectonic setting of Dire Dawa (southern Afar, Ethiopia). In: Asrat, A., Dramis, F., Nyssen, J., Umer, M. (Eds.), Geomorphology for Human Adaptation to Changing Tropical Environments. Presented at the Proceedings of the IAG/AIG Regional Conference 2011. International Association of Geomorphologists, Addis Ababa, Ethiopia, p. 41.

Coltorti, M., Pizzi, A., Abebe, B., Disperati, L., Firuzabadi, D., Pomposo, G., Sacchi, G., Salvini, R., 2011b. Geomorphology of the southern border of Afar in the Dire Dawa district (Ethiopia). In: Asrat, A., Dramis, F., Nyssen, J., Umer, M. (Eds.), Geomorphology for Human Adaptation to Changing Tropical Environments. Presented at the Proceedings of the IAG/AIG Regional Conference 2011. International Association of Geomorphologists, Addis Ababa, Ethiopia, p. 42.

de la Torre, I., Mora, R., Arroyo, A., Benito-Calvo, A., Accepted. Acheulean technological behaviour in the Middle Pleistocene landscape of Mieso (East-Central Ethiopia). J. Hum. Evol.

Deino, A.L., Scott, G.R., Saylor, B., Alene, M., Angelini, J.D., Haile-Selassie, Y., 2010. $^{40}Ar/^{39}Ar$ dating, paleomagnetism, and tephrochemistry of Pliocene strata of the hominid-bearing Woranso-Mille area, west-central Afar Rift, Ethiopia. J. Hum. Evol. 58, 111–126.

Field, L., Blundy, J., Calvert, A., Yirgu, G., 2013. Magmatic history of Dabbahu, a composite volcano in the Afar Rift, Ethiopia. Geol. Soc. Am. Bull. 125, 128–147.

Geraads, D., Alemseged, Z., Reed, D., Wynn, J.G., Roman, D., 2004. The Pleistocene fauna (other than primates) from Asbole, Lower Awash Valley, Ethiopia, and its environmental biochronological implications. Geobios 37, 697–718.

Gossa, T., Sahle, Y., Negash, A., 2012. A reassessment of the Middle and Later Stone Age lithic assemblages from Aladi Springs, Southern Afar Rift, Ethiopia. Azania: Archaeol. Res. Afr. 47, 210–222.

Juch, D., 1980. Tectonics of the southeastern escarpment of Ethiopia. Geodynamic evolution of the Afro-Arabian Rift System. Atti dei Convegni Lincei 47, 408–418.

Kidane, T., Otofuji, Y.-I., Komatsu, Y., Shibasaki, H., Yokoyama, M., 2010. Structural and geochronological implications of the Fentale Volcanics at a nascent passive margin of the Main Ethiopian Rift: Constraints from magnetostratigraphy study at the Kereyou Lodge, Ethiopia. Tectonophysics 495, 159–170.

Le Bas, M.J., Le Maitre, R.W., Streckeisen, A., Zanettin, B., IUGS Subcommission on the Systematics of Igneous Rocks, 1986. A Chemical Classification of Volcanic Rocks Based on the Total Alkali-Silica Diagram. J. Petrol 27, 745–750.

Lee, J.-Y., Marti, K., Severinghaus, J.P., Kawamura, K., Yoo, H.-S., Lee, J.B., Kim, J.S., 2006. A redetermination of the isotopic abundances of atmospheric Ar. Geochim. Cosmochim. Acta 70, 4507–4512.

Mark, D.F., Barfod, D., Stuart, F.M., Imlach, J., 2009. The ARGUS multicollector noble gas mass spectrometer: Performance for $^{40}Ar/^{39}Ar$ geochronology. Geochem. Geophys. Geosyst. 10, Q0AA02.

McBrearty, S., Brooks, A.S., 2000. The revolution that wasn't: a new interpretation of the origin of modern human behavior. J. Hum. Evol. 39, 453–563.

McHenry, L.J., Luque, L., Gómez, J.A., Diez-Martín, F., 2011. Promise and pitfalls for characterizing and correlating the zeolitically altered tephra of the Pleistocene Peninj Group, Tanzania. Quatern. Res. 75, 708–720.

Morgan, L.E., Renne, P.R., 2008. Diachronous dawn of Africa's Middle Stone Age: New $^{40}Ar/^{39}Ar$ ages from the Ethiopian Rift. Geology 36, 967–970.

Murphy, M.A., Salvador, A., 1999. International Subcommission on Stratigraphic Classification of IUGS. International Commission on Stratigraphy. International Stratigraphic Guide – An abridged version. Episodes 22, 255–271.

Quade, J., Levin, N., Semaw, Sil, Stout, D., Renne, Paul, Ros, M., Simpson, S., 2004. Paleoenvironments of the earliest stone toolmakers, Gona, Ethiopia. Geol. Soc. Am. Bull. 116, 1529–1544.

Quade, J., Levin, N.E., Simpson, S.W., Butler, R., McIntosh, W.C., Semaw, S., Kleinsasser, L., Dupont-Nivet, G., Renne, P., Dunbar, N., 2008. The geology of Gona, Afar, Ethiopia. In: Quade, J., Wynn, J.G. (Eds.), The Geology of Early Humans in the Horn of Africa, Special Paper. The Geological Society of America, pp. 1–31.

Renne, P.R., Balco, G., Ludwig, K.R., Mundil, R., Min, K., 2011. Response to the comment by W.H. Schwarz et al. on "Joint determination of ^{40}K decay constants and $^{40}Ar/^{40}K$ for the Fish Canyon sanidine standard, and improved accuracy for $^{40}Ar/^{39}Ar$ geochronology" by P.R. Renne et al. (2010). Geochim. Cosmochim. Acta 75, 5097–5100.

Sahle, Y., Morgan, L.E., Braun, D.R., Atnafu, B., Hutchings, W.K., 2014. Chronological and behavioral contexts of the earliest Middle Stone Age in the Gademotta Formation, Main Ethiopian Rift. Quatern. Int. 331, 6–19.

Schaetzl, R.J., Anderson, S., 2006. Soils: Genesis and Geomorphology. Cambridge University Press, Cambridge.

Sparks, R.S.J., Folkes, C.B., Humphreys, M.C.S., Barfod, D.N., Clavero, J., Sunagua, M.C., McNutt, S.R., Pritchard, M.E., 2008. Uturuncu volcano, Bolivia: Volcanic unrest due to mid-crustal magma intrusion. Am. J. Sci. 308, 727–769.

Suwa, G., Kono, R.T., Katoh, S., Asfaw, B., Beyene, Y., 2007. A new species of great ape from the late Miocene epoch in Ethiopia. Nature 448, 921–924.

Tefera, M., Chernet, T., Haro, W., Woldie, K., Teshome, N., 1996. Geological map of Ethiopia, scale 1:2,000,000, Second Edition. Geological Survey of Ethiopia, Ministry of Mines.

Tesfaye, S., Harding, D.J., Kusky, T.M., 2003. Early continental breakup boundary and migration of the Afar triple junction, Ethiopia. Geol. Soc. Am. Bull. 115, 1053–1067.

Tiercelin, J.J., 1990. Rift-basin sedimentation: responses to climate, tectonism and volcanism. Examples of the East African Rift. J. Afr. Earth Sci. 10, 283–305.

Ukstins, I.A., Renne, P.R., Wolfenden, E., Baker, J., Ayalew, D., Menzies, M., 2002. Matching conjugate volcanic rifted margins: $^{40}Ar/^{39}Ar$ chrono-stratigraphy of pre- and syn-rift bimodal flood volcanism in Ethiopia and Yemen. Earth Planet. Sci. Lett. 198, 289–306.

White, T.D., Asfaw, B., DeGusta, D., Gilbert, H., Richards, G.D., Suwa, G., Howell, F.C., 2003. Pleistocene *Homo sapiens* from Middle Awash, Ethiopia. Nature 423, 742–747.

Williams, M.A.J., Bishop, P.M., Dakin, F.M., Gillespie, R., 1977. Late Quaternary lake levels in southern Afar and the adjacent Ethiopian Rift. Nature 267, 690–693.

WoldeGabriel, G., 2012. Renowned paleoanthropological areas in the Ethiopian Rift basins: Geological and paleoenvironmental contexts, chronology of hominid fossils, and archaeology. In: Proceedings of the International Symposium "Africa, the Cradle of Humanity: Recent Discoveries". Travaux Du Centre National de Recherches Préhistoriques, Anthropologiques et Historiques, 18. Ministère de la Culture, Setif, Algeria, pp. 23–59.

WoldeGabriel, G., Heiken, G., White, T.D., Asfaw, B., Hart, W.K., Renne, P.R., 2000. Volcanism, tectonism, sedimentation, and the paleoanthropological record in the Ethiopian Rift System. In: McCoy, F.W., Heiken, G. (Eds.), Volcanic Hazards and Disasters in Human Antiquity. Geological Society of America Special Paper, Boulder, Colorado, pp. 83–99.

Wolfenden, E., Ebinger, C., Yirgu, G., Deino, A., Ayalew, D., 2004. Evolution of the northern Main Ethiopian rift: birth of a triple junction. Earth Planet. Sci. Lett. 224, 213–228.

Wolfenden, E., Ebinger, C., Yirgu, G., Renne, P.R., Kelley, S.P., 2005. Evolution of a volcanic rifted margin: Southern Red Sea, Ethiopia. Geol. Soc. Am. Bull. 117, 846–864.

Wynn, J.G., Roman, D.C., Alemseged, Z., Reed, D., Geraads, D., Munro, S., 2008. Stratigraphy, depositional environments, and basin structure of the Hadar and Busidima Formations at Dikika, Ethiopia. In: Quade, J., Wynn, J.G. (Eds.), The Geology of Early Humans in the Horn of Africa, Special Paper. Geol. Soc. Am., pp. 87–118.